16 Tests of the Standard Model

Over the course of the previous 15 chapters, the main elements of the Standard Model of particle physics have been described. There are 12 fundamental spin-half fermions, which satisfy the Dirac equation, and 12 corresponding antiparticles. The interactions between particles are described by the exchange of spin-1 gauge bosons where the form of the interaction is determined by the local gauge principle. The underlying gauge symmetry of the Standard Model is $\mathrm{U}(1)_Y \times \mathrm{SU}(2)_L \times \mathrm{SU}(3)$, with the electromagnetic and weak interactions described by the unified electroweak theory. The precise predictions of the electroweak theory were confronted with equally precise experimental measurements of the properties of the W and Z bosons at the LEP and Tevatron colliders. These precision tests of the Standard Model are the main subject of this chapter.

16.1 The Z resonance

The unified electroweak model introduced in Chapter 15 provides precise predictions for the properties of the Z boson. These predictions were tested with high precision at the Large Electron–Positron (LEP) collider at CERN, where large numbers of Z bosons were produced in $\mathrm{e}^+\mathrm{e}^-$ annihilation at the Z resonance.

Because the neutral Z boson couples to all flavours of fermions, the photon in any QED process can be replaced by a Z. For example, Figure 16.1 shows the two lowest-order Feynman diagrams for the annihilation process $\mathrm{e}^+\mathrm{e}^- \to \mu^+\mu^-$. The respective couplings and propagator terms that enter the matrix elements for the photon and Z exchange diagrams are

$$\mathcal{M}_\gamma \propto \frac{e^2}{q^2} \quad \text{and} \quad \mathcal{M}_\mathrm{Z} \propto \frac{g_\mathrm{Z}^2}{q^2 - m_\mathrm{Z}^2}. \tag{16.1}$$

In the s-channel annihilation process, the four-momentum of the virtual particle is equal to the centre-of-mass energy squared, $q^2 = s$. Owing to the presence of the m_Z^2 term in the Z-boson propagator, the QED process dominates at low

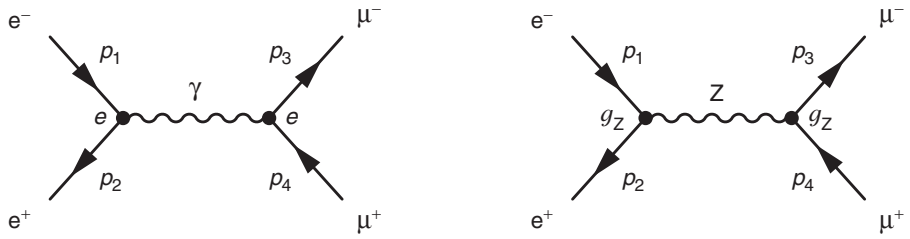

Fig. 16.1 The lowest-order Feynman diagrams for the annihilation process $e^+e^- \to \mu^+\mu^-$.

centre-of-mass energies, $\sqrt{s} \ll m_Z$. This is why the Z-boson diagram could be neglected in the discussion of electron–positron annihilation in Chapter 6. At very high centre-of-mass energies, $\sqrt{s} \gg m_Z$, the QED and Z exchange processes are both important because the strengths of the couplings of the photon and the Z boson are comparable. In the region $\sqrt{s} \sim m_Z$, the Z-boson process dominates. Indeed, from (16.1) it would appear that the matrix element diverges at $\sqrt{s} = m_Z$. This apparent problem arises because the Z-boson propagator of (16.1) does not account for the Z boson being an unstable particle.

There are a number of ways of deriving the propagator for a decaying state. Here, the form of the Z-boson propagator is obtained from the time evolution of the wavefunction for a decaying state. The time dependence of the quantum mechanical wavefunction for a stable particle, as measured in its rest frame, is given by e^{-imt}. For an unstable particle, with total decay rate $\Gamma = 1/\tau$, this must be modified to

$$\psi \propto e^{-imt} \quad \to \quad \psi \propto e^{-imt} e^{-\Gamma t/2}, \tag{16.2}$$

such that the probability density decays away as $\psi\psi^* \propto e^{-\Gamma t} = e^{-t/\tau}$. The introduction of the exponential decay term in (16.2) can be obtained from the replacement

$$m \to m - i\,\Gamma/2.$$

This suggests that the finite lifetime of the Z boson can be accounted for in the propagator of (16.1) by making the replacement

$$m_Z^2 \to (m_Z - i\,\Gamma_Z/2)^2 = m_Z^2 - i m_Z \Gamma_Z - \tfrac{1}{4}\Gamma_Z^2.$$

For the Z boson, the total decay width $\Gamma_Z \ll m_Z$, and to a good approximation the $\frac{1}{4}\Gamma_Z^2$ term can be neglected. In this case, the Z-boson propagator of (16.1) becomes

$$\frac{1}{q^2 - m_Z^2} \to \frac{1}{q^2 - m_Z^2 + i m_Z \Gamma_Z}. \tag{16.3}$$

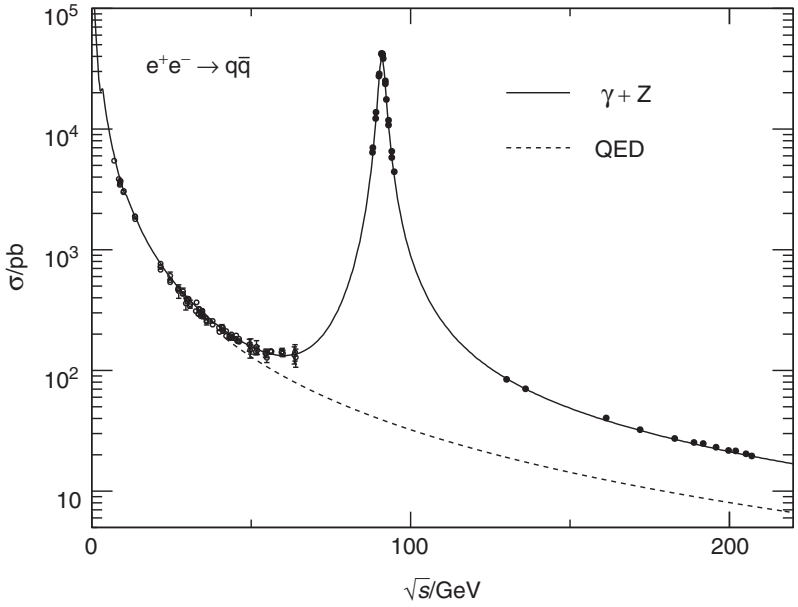

Fig. 16.2 The measurements of the $e^+e^- \to q\bar{q}$ cross section from LEP close to and above Z resonance. Also shown are the lower-energy measurements from earlier experiments. The dashed line shows the contribution to the cross section from the QED process alone. Adapted from LEP and SLD Collaborations (2006).

The cross section for $e^+e^- \to Z \to \mu^+\mu^-$, with $q^2 = s$, is therefore proportional to

$$\sigma \propto |\mathcal{M}|^2 \propto \left| \frac{1}{s - m_Z^2 + i m_Z \Gamma_Z} \right|^2 = \frac{1}{(s - m_Z^2)^2 + m_Z^2 \Gamma_Z^2}.$$

Hence the $e^+e^- \to Z$ annihilation cross section peaks sharply at $\sqrt{s} = m_Z$, and the resulting Lorentzian dependence on the centre-of-mass energy is referred to as a Breit–Wigner resonance.

The experimental measurements of the $e^+e^- \to q\bar{q}$ cross section over a wide range of centre-of-mass energies are shown in Figure 16.2. The data are compared to the prediction from the s-channel γ- and Z-exchange Feynman diagrams, including the interference between the two processes,

$$|\mathcal{M}|^2 = |\mathcal{M}_\gamma + \mathcal{M}_Z|^2.$$

The predicted cross section from the QED process alone is also shown. For centre-of-mass energies below 40 GeV, the cross section is dominated by the QED photon exchange diagram. In the region $\sqrt{s} = 50 - 80\,\text{GeV}$, both γ and Z processes are important. Close to the Z resonance, the Z-boson exchange diagram dominates; at the peak of the resonance it is about three orders of magnitude greater than pure QED contribution. For $\sqrt{s} \gg m_Z$, the contributions from the photon and Z-exchange diagrams are of the same order of magnitude, reflecting the unified description of QED and the weak interaction where $g_Z \sim e$.

16.1.1 Z production cross section

In principle, the cross section for e^+e^- annihilation close to the Z resonance, in for example the process $e^+e^- \rightarrow \mu^+\mu^-$, needs to account for the two Feynman diagrams of Figure 16.1. However, for $\sqrt{s} \sim m_Z$ the QED contribution to the total cross section can be neglected. In this case, only the matrix element for $e^+e^- \rightarrow Z \rightarrow \mu^+\mu^-$ needs to be considered. This matrix element can be obtained by using the propagator of (16.3) and the weak neutral-current vertex factor of (15.38),

$$\mathcal{M}_{fi} = -\frac{g_Z^2}{(s - m_Z^2 + im_Z\Gamma_Z)} g_{\mu\nu} \left[\overline{v}(p_2)\gamma^\mu \tfrac{1}{2}\left(c_V^e - c_A^e\gamma^5\right) u(p_1)\right] \times \left[\overline{u}(p_3)\gamma^\nu \tfrac{1}{2}\left(c_V^\mu - c_A^\mu\gamma^5\right) v(p_4)\right],$$

where c_V^e, c_A^e, c_V^μ and c_A^μ are the vector and axial-vector couplings of the Z to the electron and muon. Given the chiral nature of vector boson interactions, it is convenient to re-express this matrix element in terms of the couplings of the Z boson to left- and right-handed chiral states by writing $c_V = (c_L + c_R)$ and $c_A = (c_L - c_R)$. In this case, the matrix element can be written

$$\mathcal{M}_{fi} = -\frac{g_Z^2}{(s - m_Z^2 + im_Z\Gamma_Z)} g_{\mu\nu} \left[c_L^e \overline{v}(p_2)\gamma^\mu P_L u(p_1) + c_R^e \overline{v}(p_2)\gamma^\mu P_R u(p_1)\right] \times \left[c_L^\mu \overline{u}(p_3)\gamma^\nu P_L v(p_4) + c_R^\mu \overline{u}(p_3)\gamma^\nu P_R v(p_4)\right], \quad (16.4)$$

where $P_L = \frac{1}{2}(1-\gamma^5)$ and $P_R = \frac{1}{2}(1+\gamma^5)$ are the chiral projection operators. Given that $m_Z \gg m_\mu$, the fermions in the process $e^+e^- \rightarrow Z \rightarrow \mu^+\mu^-$ are ultra-relativistic and the helicity and chiral states are essentially the same. The chiral projection operators in (16.4) therefore have the effect

$$P_L u = u_\downarrow, \quad P_R u = u_\uparrow, \quad P_L v = v_\uparrow \quad \text{and} \quad P_R v = v_\downarrow.$$

Furthermore, as described in Section 15.4, helicity combinations such as $\overline{u}_\uparrow\gamma^\mu v_\uparrow$ give zero matrix elements. Consequently the matrix element of (16.4) is only non-zero for the four helicity combinations shown in Figure 16.3, with the corresponding matrix elements

$$\mathcal{M}_{RR} = -P_Z(s)\, g_Z^2\, c_R^e c_R^\mu\, g_{\mu\nu}\, [\overline{v}_\downarrow(p_2)\gamma^\mu u_\uparrow(p_1)]\, [\overline{u}_\uparrow(p_3)\gamma^\nu v_\downarrow(p_4)], \quad (16.5)$$

$$\mathcal{M}_{RL} = -P_Z(s)\, g_Z^2\, c_R^e c_L^\mu\, g_{\mu\nu}\, [\overline{v}_\downarrow(p_2)\gamma^\mu u_\uparrow(p_1)]\, [\overline{u}_\downarrow(p_3)\gamma^\nu v_\uparrow(p_4)], \quad (16.6)$$

$$\mathcal{M}_{LR} = -P_Z(s)\, g_Z^2\, c_L^e c_R^\mu\, g_{\mu\nu}\, [\overline{v}_\uparrow(p_2)\gamma^\mu u_\downarrow(p_1)]\, [\overline{u}_\uparrow(p_3)\gamma^\nu v_\downarrow(p_4)], \quad (16.7)$$

$$\mathcal{M}_{LL} = -P_Z(s)\, g_Z^2\, c_L^e c_L^\mu\, g_{\mu\nu}\, [\overline{v}_\uparrow(p_2)\gamma^\mu u_\downarrow(p_1)]\, [\overline{u}_\downarrow(p_3)\gamma^\nu v_\uparrow(p_4)], \quad (16.8)$$

where $P_Z(s) = 1/(s - m_Z^2 + im_Z\Gamma_Z)$ is the Z propagator and the labels on the different matrix elements $\mathcal{M}$ denote the helicity states of the e^- and μ^-.

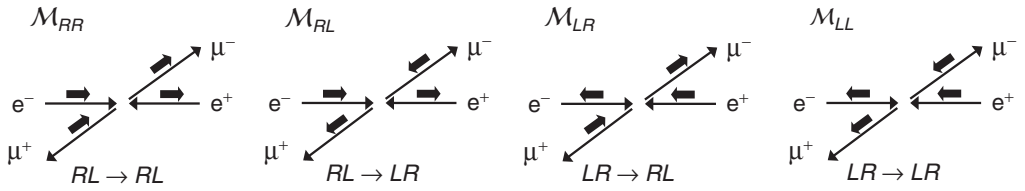

Fig. 16.3 The four possible helicity combinations contributing to $e^+e^- \to Z \to \mu^+\mu^-$. The corresponding matrix elements are labelled by the helicity states of the e^- and μ^-.

The combinations of four-vector currents in (16.5)–(16.8) are identical to those encountered in Chapter 6 for the pure QED process $e^+e^- \to \mu^+\mu^-$, where for example

$$g_{\mu\nu}[\overline{v}_\downarrow(p_2)\gamma^\mu u_\uparrow(p_1)][\overline{u}_\uparrow(p_3)\gamma^\nu v_\downarrow(p_4)] = s(1+\cos\theta).$$

Using the previously derived results of (6.20) and (6.21), the matrix elements squared for the four helicity combinations in the process $e^+e^- \to Z \to \mu^+\mu^-$ are

$$|\mathcal{M}_{RR}|^2 = |P_Z(s)|^2\, g_Z^4 s^2 (c_R^e)^2 (c_R^\mu)^2 (1+\cos\theta)^2, \tag{16.9}$$
$$|\mathcal{M}_{RL}|^2 = |P_Z(s)|^2\, g_Z^4 s^2 (c_R^e)^2 (c_L^\mu)^2 (1-\cos\theta)^2, \tag{16.10}$$
$$|\mathcal{M}_{LR}|^2 = |P_Z(s)|^2\, g_Z^4 s^2 (c_L^e)^2 (c_R^\mu)^2 (1-\cos\theta)^2, \tag{16.11}$$
$$|\mathcal{M}_{LL}|^2 = |P_Z(s)|^2\, g_Z^4 s^2 (c_L^e)^2 (c_L^\mu)^2 (1+\cos\theta)^2, \tag{16.12}$$

where $|P_Z(s)|^2 = 1/[(s-m_Z^2)^2 + m_Z^2\Gamma_Z^2]$.

For unpolarised e^- and e^+ beams, the spin-averaged matrix element is given by

$$\langle|\mathcal{M}|^2\rangle = \frac{1}{4}\left(|\mathcal{M}_{RR}|^2 + |\mathcal{M}_{LL}|^2 + |\mathcal{M}_{LR}|^2 + |\mathcal{M}_{RL}|^2\right),$$

where the factor of one quarter arises from averaging over the two possible helicity states for each of the electron and the positron, and therefore from (16.9)–(16.12),

$$\langle|\mathcal{M}|^2\rangle = \frac{1}{4}\frac{g_Z^4 s^2}{(s-m_Z^2)^2 + m_Z^2\Gamma_Z^2} \times \Big\{\Big[(c_R^e)^2(c_R^\mu)^2 + (c_L^e)^2(c_L^\mu)^2\Big](1+\cos\theta)^2 + \Big[(c_R^e)^2(c_L^\mu)^2 + (c_L^e)^2(c_R^\mu)^2\Big](1-\cos\theta)^2\Big\}. \tag{16.13}$$

The terms in the braces can be grouped into

$$\{\cdots\} = \Big[(c_R^e)^2 + (c_L^e)^2\Big]\Big[(c_R^\mu)^2 + (c_L^\mu)^2\Big]\Big(1+\cos^2\theta\Big) + 2\Big[(c_R^e)^2 - (c_L^e)^2\Big]\Big[(c_R^\mu)^2 - (c_L^\mu)^2\Big]\cos\theta, \tag{16.14}$$

which can then be expressed back in terms of the vector and axial-vector couplings of the electron and muon to the Z boson using

$$c_V^2 + c_A^2 = 2(c_L^2 + c_R^2) \quad \text{and} \quad c_V c_A = c_L^2 - c_R^2,$$

giving

$$\{\ldots\} = \tfrac{1}{4}\left[(c_V^{\mathrm{e}})^2 + (c_A^{\mathrm{e}})^2\right]\left[(c_V^{\mu})^2 + (c_A^{\mu})^2\right]\left(1 + \cos^2\theta\right) + 2c_V^{\mathrm{e}}c_A^{\mathrm{e}}c_V^{\mu}c_A^{\mu}\cos\theta.$$

Finally, the $\mathrm{e}^+\mathrm{e}^- \to \mathrm{Z} \to \mu^+\mu^-$ differential cross section is obtained by substituting the spin-averaged matrix element squared into (3.50),

$$\frac{\mathrm{d}\sigma}{\mathrm{d}\Omega} = \frac{1}{256\pi^2 s} \cdot \frac{g_{\mathrm{Z}}^4 s^2}{(s - m_{\mathrm{Z}}^2)^2 + m_{\mathrm{Z}}^2\Gamma_{\mathrm{Z}}^2} \times \left\{\tfrac{1}{4}\left[(c_V^{\mathrm{e}})^2 + (c_A^{\mathrm{e}})^2\right]\left[(c_V^{\mu})^2 + (c_A^{\mu})^2\right]\left(1 + \cos^2\theta\right) + 2c_V^{\mathrm{e}}c_A^{\mathrm{e}}c_V^{\mu}c_A^{\mu}\cos\theta\right\}. \quad (16.15)$$

The total cross section is determined by integrating over the solid angle $\mathrm{d}\Omega$. This is most easily performed by writing $\mathrm{d}\Omega = \mathrm{d}\phi\,\mathrm{d}(\cos\theta)$ and making the substitution $x = \cos\theta$, such that

$$\int (1 + \cos^2\theta)\,\mathrm{d}\Omega = \int_0^{2\pi} \mathrm{d}\phi \int_{-1}^{+1} (1 + x^2)\,\mathrm{d}x = \frac{16\pi}{3} \quad \text{and} \quad \int \cos\theta\,\mathrm{d}\Omega = 0.$$

The resulting cross section for the process $\mathrm{e}^+\mathrm{e}^- \to \mathrm{Z} \to \mu^+\mu^-$ is

$$\sigma(\mathrm{e}^+\mathrm{e}^- \to \mathrm{Z} \to \mu^+\mu^-) = \frac{1}{192\pi} \frac{g_{\mathrm{Z}}^4 s}{(s - m_{\mathrm{Z}}^2)^2 + m_{\mathrm{Z}}^2\Gamma_{\mathrm{Z}}^2} \left[(c_V^{\mathrm{e}})^2 + (c_A^{\mathrm{e}})^2\right]\left[(c_V^{\mu})^2 + (c_A^{\mu})^2\right].$$

Thus, the total $\mathrm{e}^+\mathrm{e}^- \to \mathrm{Z} \to \mu^+\mu^-$ cross section is proportional to the product of the sum of the squares of the vector and axial-vector couplings of the initial-state electrons and the final-state muons. Using the expression for the partial decay widths of the Z boson, given in (15.41), the sums $c_V^2 + c_A^2$ for the electron and muon can be related to $\Gamma_{\mathrm{ee}} = \Gamma(\mathrm{Z} \to \mathrm{e}^+\mathrm{e}^-)$ and $\Gamma_{\mu\mu} = \Gamma(\mathrm{Z} \to \mu^+\mu^-)$,

$$\Gamma_{\mathrm{ee}} = \frac{g_{\mathrm{Z}}^2 m_{\mathrm{Z}}}{48\pi}\left[(c_V^{\mathrm{e}})^2 + (c_A^{\mathrm{e}})^2\right] \quad \text{and} \quad \Gamma_{\mu\mu} = \frac{g_{\mathrm{Z}}^2 m_{\mathrm{Z}}}{48\pi}\left[(c_V^{\mu})^2 + (c_A^{\mu})^2\right].$$

Hence, the total cross section, expressed in terms of the partial decay widths, is

$$\sigma(\mathrm{e}^+\mathrm{e}^- \to \mathrm{Z} \to \mu^+\mu^-) = \frac{12\pi s}{m_{\mathrm{Z}}^2} \frac{\Gamma_{\mathrm{ee}}\Gamma_{\mu\mu}}{(s - m_{\mathrm{Z}}^2)^2 + m_{\mathrm{Z}}^2\Gamma_{\mathrm{Z}}^2}. \quad (16.16)$$

The cross sections for other final-state fermions are given by simply replacing $\Gamma_{\mu\mu}$ by the partial width $\Gamma_{\mathrm{ff}} = \Gamma(\mathrm{e}^+\mathrm{e}^- \to \mathrm{f}\bar{\mathrm{f}})$.

The properties of the Z resonance are described by (16.16). The maximum value of the cross section, which occurs at the centre-of-mass energy $\sqrt{s} = m_{\mathrm{Z}}$, is

$$\sigma_{\mathrm{ff}}^0 = \frac{12\pi}{m_{\mathrm{Z}}^2} \frac{\Gamma_{\mathrm{ee}}\Gamma_{\mathrm{ff}}}{\Gamma_{\mathrm{Z}}^2}. \quad (16.17)$$

From (16.16) it is straightforward to show that the cross section falls to half of its peak value at

$$\sqrt{s} = m_Z \pm \Gamma_Z/2.$$

Therefore Γ_Z is not only the total decay rate of the Z boson, it is also the full-width-at-half-maximum (FWHM) of the cross section as a function of centre-of-mass energy. Hence the mass and total width of the Z boson can be determined directly from measurements of the centre-of-mass energy dependence of the cross section for $e^+e^- \to Z \to f\bar{f}$. Furthermore, once m_Z and Γ_Z are known, the measured value of peak cross section for a particular final-state fermion σ^0_{ff} can be related to the product of the partial decay widths using (16.17),

$$\Gamma_{ee}\Gamma_{ff} = \frac{\sigma^0_{ff}\Gamma_Z^2 m_Z^2}{12\pi}.$$

Hence, the observed peak cross sections can be used to determine the partial decay widths of the Z boson for the different visible final states.

16.2 The Large Electron–Positron collider

The LEP collider, which operated at CERN from 1989 to 2000, is the highest energy electron–positron collider ever built. The circular accelerator was located in the 26 km circumference underground tunnel that is now home to the LHC. The electrons and positrons circulated in opposite directions and collided at four interaction points, spaced equally around the ring, accommodating four large general purpose detectors, ALEPH, DELPHI, L3 and OPAL. From 1989 to 1995, LEP operated at centre-of-mass energies close to the Z mass and the four experiments accumulated over 17 million Z events between them, allowing its properties to be determined with high precision. From 1996 to 2000, LEP operated above the threshold for W^+W^- production and the LEP experiments accumulated a total of more than 30 000 $e^+e^- \to W^+W^-$ events over the centre-of-mass energy range 161–208 GeV, allowing the properties of the W boson to be studied in detail.

16.2.1 Measurement of the mass and width of the Z

At LEP, the mass and width of the Z boson were determined from the centre-of-mass energy dependence of the measured $e^+e^- \to Z \to q\bar{q}$ cross section. In principle, the cross section is described by the Breit–Wigner resonance of (16.16), with the maximum occurring at $\sqrt{s} = m_Z$ and the FWHM giving Γ_Z. In practice, this is not quite the case. In addition to the lowest-order Feynman diagram, there are two higher-order QED diagrams where a photon is radiated from either the

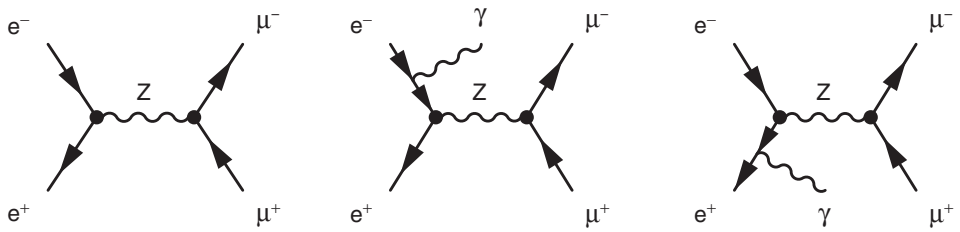

Fig. 16.4 The lowest-order Feynman diagram for the annihilation process $e^+e^- \to \mu^+\mu^-$ and the diagrams including initial-state radiation.

initial-state electron or positron, as shown in Figure 16.4. The effect of initial-state radiation (ISR) is to distort the shape of the Z resonance curve. If an ISR photon with energy E_γ is radiated, the energy of the e^+ or e^- is reduced from E to $E' = E - E_\gamma$, where E is the nominal energy of the electron and positron beams. In the limit where the photon is emitted collinear with the incoming electron/positron (which is usually the case), the four-momenta of the electron and positron at the Z production vertex are $p_1 = (E - E_\gamma, 0, 0, E - E_\gamma)$ and $p_2 = (E, 0, 0, -E)$. For collisions at a nominal centre-of-mass energy of $\sqrt{s}$, the effect of ISR is to produce a distribution of the four-momentum q_Z of the virtual Z bosons. This can be expressed as the effective centre-of-mass energy squared at the e^+e^- annihilation vertex $s' = q_Z^2$, given by the square of the sum of four-momenta of the e^+ and e^- after ISR,

$$s' = (p_1 + p_2)^2 = (2E - E_\gamma)^2 - E_\gamma^2 = 4E^2\left(1 - \frac{E_\gamma}{E}\right) = s\left(1 - \frac{E_\gamma}{E}\right).$$

The impact of ISR is to reduce the effective centre-of-mass energy for the collisions where ISR photons are emitted; even if the accelerator is operated at a nominal centre-of-mass energy equal to m_Z, some fraction of the Z bosons will be produced with $q_Z^2 < m_Z^2$.

The distribution of $\sqrt{s'}$ can be written in terms of the normalised probability distribution $f(s', s)$. The measured cross section is the convolution of the s' distribution with the cross section $\sigma(s')$ obtained from (16.16),

$$\sigma_{\text{meas}}(s) = \int \sigma(s') f(s', s)\, \mathrm{d}s'.$$

The effect of ISR is to distort the measured Z resonance. However, because ISR is a QED process, the function $f(s', s)$ can be calculated to high precision. Consequently, the measured cross section can be corrected back to the underlying Breit–Wigner distribution. Figure 16.5 shows the measured $e^+e^- \to Z \to q\bar{q}$ cross section as a function of centre-of-mass energy. The data are compared to the expected distribution including ISR. The dashed curve shows the reconstructed shape of the Z resonance after the deconvolution of the effects of ISR. Close to and below the peak of the resonance, ISR results in a reduction in the measured cross section because the centre-of-mass energy at the e^+e^- vertex is moved further from the peak of

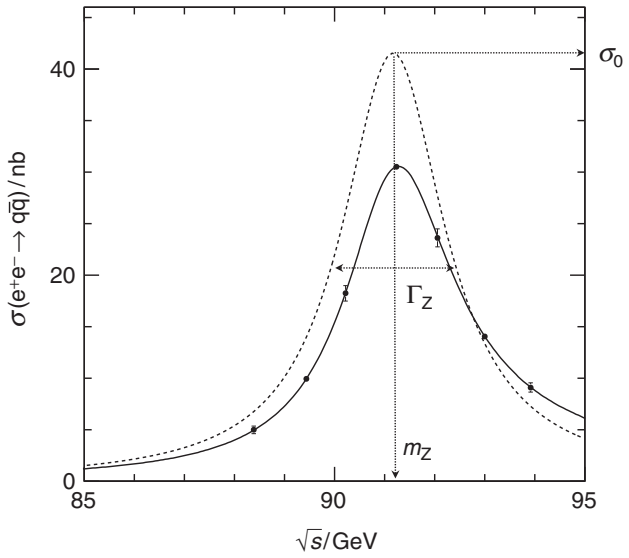

Fig. 16.5 The measurements of the $e^+e^- \to q\bar{q}$ cross section from LEP close to the Z resonance. The expected resonance curves, before and after correcting for ISR are shown by the solid and dashed lines respectively. The measurement errors have been multiplied by a factor of 10 to improve visibility. Adapted from LEP and SLD Collaborations (2006).

the resonance. Above the peak of the resonance, ISR increases the cross section because the average centre-of-mass energy is moved closer to the peak.

From the measurements of the Z resonance at LEP, shown in Figure 16.5, the mass of the Z boson is determined to be

$$m_Z = 91.1875 \pm 0.0021\,\text{GeV}.$$

Owing to the large numbers of Z bosons produced at LEP, m_Z could be measured with a precision of 0.002%, making it one of the more precisely known fundamental parameters. To achieve this high level of precision, the average centre-of-mass energy of the LEP collider had to be known to 2 MeV. This required a detailed understanding of a number of potential systematic biases. For example, tidal effects due to the gravitational pull of the Moon distort the rock surrounding the LEP accelerator by a small amount, resulting in ±0.15 mm variations in the 4.3 km radius of the accelerator. These variations are sufficient to change the beam energy by approximately ±10 MeV. Nevertheless, the position of the Moon is known and the effect of these tidal variations could be accounted for. A more subtle and unexpected effect was the observation of apparent jumps in the beam energies at specific times of the day. After much investigation, the origin was identified as leakage currents from the local high-speed railway. These leakage currents followed the path of least resistance in a circuit formed from the rails, a local river and the LEP ring. The small currents that ran along the LEP ring, were sufficient to

modify the magnetic field in the accelerator, leading to small changes in the beam energy. Once understood, the affected data could be treated appropriately.

The width of the Z-boson

The total width of the Z boson, determined from the FWHM of the Breit–Wigner resonance curve after unfolding the effects of ISR (shown in Figure 16.5) is

$$\Gamma_Z = 2.4952 \pm 0.0023\,\text{GeV},$$

corresponding to a lifetime of just 2.6×10^{-25} s. The total width of the Z is the sum of the partial decay widths for all its decay modes,

$$\Gamma_Z = \Gamma_{ee} + \Gamma_{\mu\mu} + \Gamma_{\tau\tau} + \Gamma_{\text{hadrons}} + \Gamma_{\nu_e\nu_e} + \Gamma_{\nu_\mu\nu_\mu} + \Gamma_{\nu_\tau\nu_\tau}, \tag{16.18}$$

where Γ_{hadrons} is the partial decay width to all final states with quarks. Assuming the lepton universality of the weak neutral-current, (16.18) can be written

$$\Gamma_Z = 3\Gamma_{\ell\ell} + \Gamma_{\text{hadrons}} + 3\Gamma_{\nu\nu},$$

where $\Gamma_{\ell\ell}$ and $\Gamma_{\nu\nu}$ are respectively the partial decay widths to a single flavour of charged lepton or neutrino. Although the decays to neutrinos are not observed, they still affect the observable total width of the Z resonance.

To date only three generations of fermions have been observed. This in itself does not preclude the possibility of a fourth generation, provided the fourth-generation particles are sufficiently massive to have avoided detection. However, if there were a fourth-generation neutrino, with similar properties to the three known generations, the neutrino would be sufficiently light for the decay $Z \to \nu_4\bar{\nu}_4$ to occur. This possibility can be tested through its observable effect on Γ_Z. For N_ν light neutrino generations, the expected width of the Z boson is

$$\Gamma_Z = 3\Gamma_{\ell\ell} + \Gamma_{\text{hadrons}} + N_\nu\Gamma_{\nu\nu}. \tag{16.19}$$

Hence the number of light neutrino generations that exist in nature can be obtained from the measured values of Γ_Z, $\Gamma_{\ell\ell}$ and Γ_{hadrons} using

$$N_\nu = \frac{(\Gamma_Z - 3\Gamma_{\ell\ell} - \Gamma_{\text{hadrons}})}{\Gamma_{\nu\nu}^{\text{SM}}}, \tag{16.20}$$

where $\Gamma_{\nu\nu}^{\text{SM}}$ is the Standard Model prediction of (15.42). The individual partial decay widths to particles other than neutrinos, can be determined from the measured cross sections at the peak of the Z resonance using

$$\sigma^0(e^+e^- \to Z \to f\bar{f}) = \frac{12\pi}{m_Z^2}\frac{\Gamma_{ee}\Gamma_{ff}}{\Gamma_Z^2}. \tag{16.21}$$

Given that m_Z and Γ_Z are known precisely, the measured peak cross section for $e^+e^- \to Z \to e^+e^-$ determines Γ_{ee}^2. Once Γ_{ee} is known, the partial decay widths of

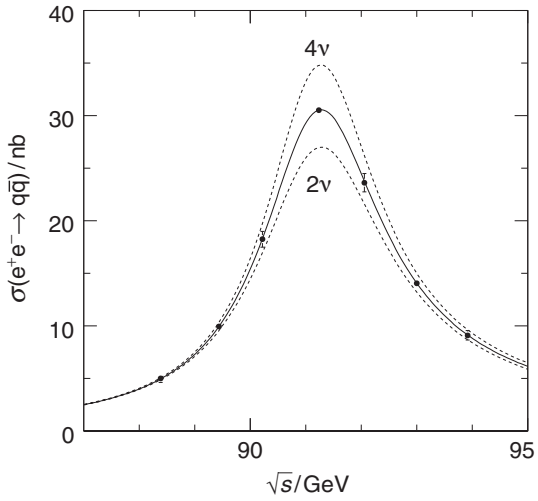

Fig. 16.6 The measurements of the $e^+e^- \rightarrow q\bar{q}$ cross section from LEP close to the Z resonance compared to the Standard Model expectation for two, three and four light neutrino generations. Adapted from LEP and SLD Collaborations (2006).

the Z boson to the other visible final states can be determined from the respective peak cross sections, again using (16.21). Using the measured values of the partial decay widths and the relation of (16.20), the number of light neutrino generations is determined to be

$$N_\nu = 2.9840 \pm 0.0082. \tag{16.22}$$

Figure 16.6 compares the measured $e^+e^- \rightarrow q\bar{q}$ cross section, close to the Z resonance, with the expected cross sections for two, three and four neutrino generations. The consistency of the data with the predictions for three neutrino generations provides strong evidence that there are exactly three generations of light neutrinos (assuming Standard Model couplings) from which it can be inferred that there are probably only three generations of fermions.

16.2.2 Measurements of the weak mixing angle

The weak mixing angle θ_W is one of the fundamental parameters of the Standard Model. The Standard Model vector and axial-vector couplings of the fermions to the Z boson are given by (15.36) and (15.37),

$$c_V = I_W^{(3)} - 2Q \sin^2 \theta_W \quad \text{and} \quad c_A = I_W^{(3)},$$

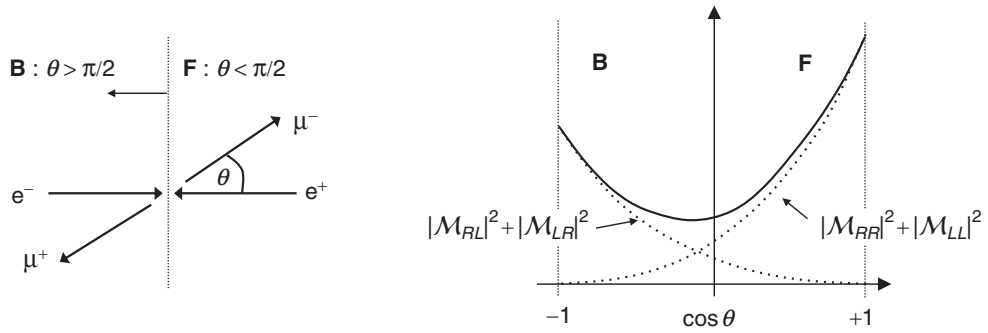

Fig. 16.7 The definition of the forward ($\theta_{\mu^-} < \pi/2$) and backward ($\theta_{\mu^-} > \pi/2$) hemispheres and the contributions to the differential cross section from the different helicity combinations.

and thus $\sin^2\theta_{\mathrm{W}}$ can be obtained from measurements of c_V. In practice, the relevant experimental observables depend on the ratio of couplings,

$$\frac{c_V}{c_A} = 1 - \frac{2Q\sin^2\theta_{\mathrm{W}}}{I_{\mathrm{W}}^{(3)}}.$$

For the charged leptons, with $Q = -1$ and $I_{\mathrm{W}}^{(3)} = -1/2$,

$$\frac{c_V^\ell}{c_A^\ell} = 1 - 4\sin^2\theta_{\mathrm{W}}. \tag{16.23}$$

There are a number of ways in which the ratio c_V/c_A can be obtained from measurements at LEP. The simplest conceptually is the measurement of the forward–backward asymmetry A_{FB} of the leptons produced in $\mathrm{e^+e^-} \to \mathrm{Z} \to \ell^+\ell^-$. A_{FB} reflects the asymmetry in angular distribution of the final-state leptons and is defined as

$$A_{\mathrm{FB}}^\ell = \frac{\sigma_F - \sigma_B}{\sigma_F + \sigma_B}. \tag{16.24}$$

Here σ_F and σ_B are the respective cross sections for the negatively charged lepton being produced in the forward ($\theta_{\ell^-} < \pi/2$) and backward ($\theta_{\ell^-} > \pi/2$) hemispheres, as indicated in Figure 16.7.

The differential cross section for $\mathrm{e^+e^-} \to \mathrm{Z} \to \mu^+\mu^-$ of (16.14) has the form

$$\frac{\mathrm{d}\sigma}{\mathrm{d}\Omega} \propto a(1 + \cos^2\theta) + 2b\cos\theta, \tag{16.25}$$

where the coefficients a and b are given by

$$a = \left[(c_L^{\mathrm{e}})^2 + (c_R^{\mathrm{e}})^2\right]\left[(c_L^{\mu})^2 + (c_R^{\mu})^2\right] \quad \text{and} \quad b = \left[(c_L^{\mathrm{e}})^2 - (c_R^{\mathrm{e}})^2\right]\left[(c_L^{\mu})^2 - (c_R^{\mu})^2\right].$$

If the couplings of the Z boson to left-handed (LH) and right-handed (RH) fermions were the same, b would be equal to zero and the angular distribution would have

the symmetric $(1+\cos^2\theta)$ form seen previously for the pure QED process, in which case $A_{\rm FB} = 0$.

The different couplings of the Z boson to LH and RH fermions manifests itself in differences in the magnitudes of the squared matrix elements for the four helicity combinations of Figure 16.3. From (16.9)–(16.12), it can be seen that the sum of the squared matrix elements for the $RL \to RL$ and $LR \to LR$ helicity combinations depends on $(1 + \cos\theta)^2$, whereas the sum for the $RL \to LR$ and $LR \to RL$ combinations depends on $(1 - \cos\theta)^2$. This difference results in a forward–backward asymmetry in the differential cross section, as indicated in the right-hand plot of Figure 16.7.

The forward and backward cross sections, σ_F and σ_B, can be obtained by integrating the differential cross section of (16.25) over the two different polar angle ranges, $0 < \theta < \pi/2$ and $\pi/2 < \theta < \pi$. Writing $\mathrm{d}\Omega = \mathrm{d}\phi\,\mathrm{d}(\cos\theta)$,

$$\sigma_F \equiv 2\pi \int_0^1 \frac{\mathrm{d}\sigma}{\mathrm{d}\Omega}\mathrm{d}(\cos\theta) \quad \text{and} \quad \sigma_B \equiv 2\pi \int_{-1}^0 \frac{\mathrm{d}\sigma}{\mathrm{d}\Omega}\mathrm{d}(\cos\theta).$$

From the form of the differential cross section of (16.25), σ_F and σ_B are

$$\sigma_F \propto \int_0^1 \Big[a(1+\cos^2\theta) + 2b\cos\theta\Big]\,\mathrm{d}(\cos\theta) = \int_0^1 \Big[a(1+x^2) + 2bx\Big]\,\mathrm{d}x = \Big(\tfrac{4}{3}a + b\Big),$$

$$\sigma_B \propto \int_{-1}^0 \Big[a(1+\cos^2\theta) + 2b\cos\theta\Big]\,\mathrm{d}(\cos\theta) = \int_{-1}^0 \Big[a(1+x^2) + 2bx\Big]\,\mathrm{d}x = \Big(\tfrac{4}{3}a - b\Big).$$

Thus the forward–backward asymmetry is given by

$$A_{\rm FB} = \frac{\sigma_F - \sigma_B}{\sigma_F + \sigma_B} = \frac{3b}{4a}.$$

From the expressions for the coefficients a and b, the forward–backward asymmetry is related to the left- and right-handed couplings of the fermions by

$$A_{\rm FB} = \frac{3}{4}\left[\frac{(c_L^{\rm e})^2 - (c_R^{\rm e})^2}{(c_L^{\rm e})^2 + (c_R^{\rm e})^2}\right]\cdot\left[\frac{(c_L^{\mu})^2 - (c_R^{\mu})^2}{(c_L^{\mu})^2 + (c_R^{\mu})^2}\right].$$

This can be written in the form

$$A_{\rm FB} = \frac{3}{4}\mathcal{A}_{\rm e}\mathcal{A}_{\mu},$$

where the asymmetry parameter $\mathcal{A}_{\rm f}$ for a particular flavour f is defined by

$$\mathcal{A}_{\rm f} = \frac{(c_L^{\rm f})^2 - (c_R^{\rm f})^2}{(c_L^{\rm f})^2 + (c_R^{\rm f})^2} \equiv \frac{2c_V^{\rm f}c_A^{\rm f}}{(c_V^{\rm f})^2 + (c_A^{\rm f})^2}. \tag{16.26}$$

At LEP, $A_{\rm FB}$ is most cleanly measured using the $\mathrm{e^+e^-}$, $\mu^+\mu^-$ and $\tau^+\tau^-$ final states, where the charges of the leptons are determined from the sense of the curvature of the measured particle track in the magnetic field of the detector. By counting the

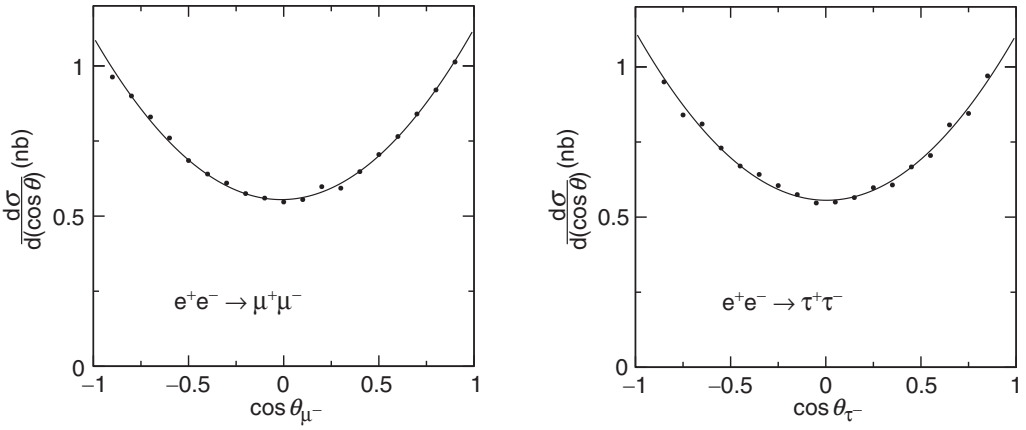

Fig. 16.8 Measurements of the differential cross sections for $e^+e^- \to \mu^+\mu^-$ and $e^+e^- \to \tau^+\tau^-$ at $\sqrt{s} = m_Z$. Adapted from the OPAL Collaboration, Abbiendi *et al.* (2001).

numbers of events where the ℓ^- is produced in either the forward or backward hemispheres, N_F and N_B, the measured forward–backward asymmetry is simply

$$A_{\rm FB} = \frac{N_F - N_B}{N_F + N_B}.$$

In the measurement of $A_{\rm FB}$, many potential systematic biases cancel because they tend to affect both forward and backward events in the same manner, consequently a precise measurement can be made. In practice, $A_{\rm FB}$ is obtained from the observed angular distribution, rather than simply counting events. For example, Figure 16.8 shows the OPAL measurements of the $e^+e^- \to \mu^+\mu^-$ and $e^+e^- \to \tau^+\tau^-$ differential cross sections at $\sqrt{s} = m_Z$. The observed asymmetry is small, but non-zero.

Combining the results from the four LEP experiments gives

$$A^{\rm e}_{FB} = 0.0145 \pm 0.0025, \quad A^{\mu}_{FB} = 0.0169 \pm 0.0013 \quad \text{and} \quad A^{\tau}_{FB} = 0.0188 \pm 0.0017.$$

These measurements can be expressed in terms of the asymmetry parameter defined in (16.26), giving

$$A^{\rm e}_{FB} = \frac{3}{4}\mathcal{A}_{\rm e}^2, \quad A^{\mu}_{FB} = \frac{3}{4}\mathcal{A}_{\rm e}\mathcal{A}_{\mu} \quad \text{and} \quad A^{\tau}_{FB} = \frac{3}{4}\mathcal{A}_{\rm e}\mathcal{A}_{\tau}.$$

Hence the measurements of the forward–backward asymmetries can be interpreted as measurements of the asymmetry parameters for the individual lepton flavours, with the $e^+e^- \to Z \to e^+e^-$ process uniquely determining $\mathcal{A}_{\rm e}$.

There are a number of other ways of measuring the lepton asymmetry parameters at LEP and elsewhere. For example, the results from the left-right asymmetry measured in the SLD detector at the Stanford Linear Collider (SLC) provides a precise measurement of $\mathcal{A}_{\rm e}$ alone (see Problem 16.4). The combined results from LEP and SLC give

$$\mathcal{A}_e = 0.1514 \pm 0.0019, \quad \mathcal{A}_\mu = 0.1456 \pm 0.0091 \quad \text{and} \quad \mathcal{A}_\tau = 0.1449 \pm 0.0040,$$

consistent with the lepton universality of the weak neutral-current.

Dividing both the numerator and denominator of (16.26) by c_A^2 gives the expression for the asymmetry parameters in terms of c_V/c_A,

$$\mathcal{A} = \frac{2c_V/c_A}{1 + (c_V/c_A)^2}.$$

Therefore, the measured asymmetry parameters for the leptons can be interpreted as measurements of c_V/c_A, which then can be related to $\sin^2\theta_W$ using (16.23),

$$\frac{c_V}{c_A} = 1 - 4\sin^2\theta_W.$$

When the various measurements of $\sin^2\theta_W$ from the Z resonance and elsewhere are combined, the weak mixing angle is determined to be

$$\sin^2\theta_W = 0.23146 \pm 0.00012.$$

The lepton forward–backward asymmetries are small because $\sin^2\theta_W$ is nearly 1/4.

16.3 Properties of the W boson

The studies of the Z boson provide a number of important results, including the precise measurements of m_Z, Γ_Z and $\sin^2\theta_W$. Further constraints on the electroweak sector of the Standard Model can be obtained from studies of the W boson. From 1996 to 2000, the LEP collider operated at $\sqrt{s} > 161\,\text{GeV}$, above the threshold for production of $e^+e^- \to W^+W^-$. In $e^+e^- \to W^+W^-$ events, each W boson can decay either leptonically, for example $W^- \to \mu^-\overline{\nu}_\mu$, or hadronically, for example $W^- \to d\overline{u}$. Consequently, $e^+e^- \to W^+W^-$ interactions at LEP are observed in the three distinct event topologies shown in Figure 16.9. Events where both W bosons decay leptonically are observed as two charged leptons and an imbalance of momentum in the transverse plane due to the two unseen neutrinos. Events where one W decays leptonically and the other decays hadronically are observed as two jets, a single charged lepton and an imbalance of momentum from the neutrino. Finally, events where both W bosons decay hadronically produce four jets. The distinctive event topologies enable $e^+e^- \to W^+W^-$ events to be identified with high efficiency and little ambiguity.

The observed numbers of events in each of the three W^+W^- topologies can be related to branching ratio for $W \to q\overline{q}'$. For example, the numbers of fully hadronic decays and fully leptonic decays are respectively proportional to

$$N_{qqqq} \propto \left[BR(W \to q\overline{q}')\right]^2 \quad \text{and} \quad N_{\ell\nu\ell\nu} \propto \left[1 - BR(W \to q\overline{q}')\right]^2.$$

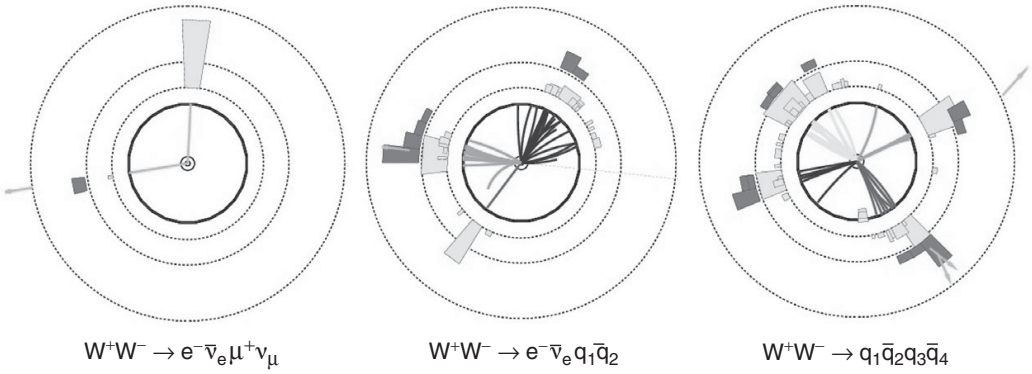

Fig. 16.9 The three possible event topologies for the decays of W^+W^- in $e^+e^- \to W^+W^-$ at LEP. Reproduced courtesy of the OPAL Collaboration.

Consequently, the relative numbers of observed events in the three W^+W^- topologies gives a precise measurement of the W-boson branching ratio to hadrons,

$$BR(W \to q\bar{q}') = 67.41 \pm 0.27\%.$$

This is consistent with the Standard Model expectation of 67.5% obtained from (15.9). Furthermore, the decays $W \to e\nu$, $W \to \mu\nu$ and $W \to \tau\nu$ are observed to occur with equal frequencies, consistent with the expectation from the lepton universality of the charged-current weak interaction.

Figure 16.10 shows the combined measurements of the $e^+e^- \to W^+W^-$ cross section from the four LEP experiments. The data are consistent with the Standard Model expectation determined from the three Feynman diagrams of Figure 15.5. The contribution to the total cross section from the *s*-channel Z-exchange diagram, shown in Figure 16.11, depends on the strength of the W^+W^-Z coupling, which in the Standard Model is fixed by the local gauge symmetry and the electroweak unification mechanism. The predicted cross section without the contribution from the Z-exchange diagram, also shown in Figure 16.10, clearly does not reproduce the data. The $e^+e^- \to W^+W^-$ cross section measurements therefore provide a test the Standard Model prediction of the strength of coupling at the W^+W^-Z vertex. Yet again, the Standard Model provides an excellent description of the data.

16.3.1 Measurement of the W boson mass and width

The mass and width of the Z boson are determined from the shape of the resonance in the Z production cross section in e^+e^- collisions. The production of W-pairs at LEP is not a resonant process; for $\sqrt{s} > 2m_W$, the Z boson in the *s*-channel Feynman diagram of Figure 16.11 is far from being on-mass shell. Consequently different techniques are required to measure the mass and width of the W boson. In principle, it is possible to measure the W boson mass and width from the shape

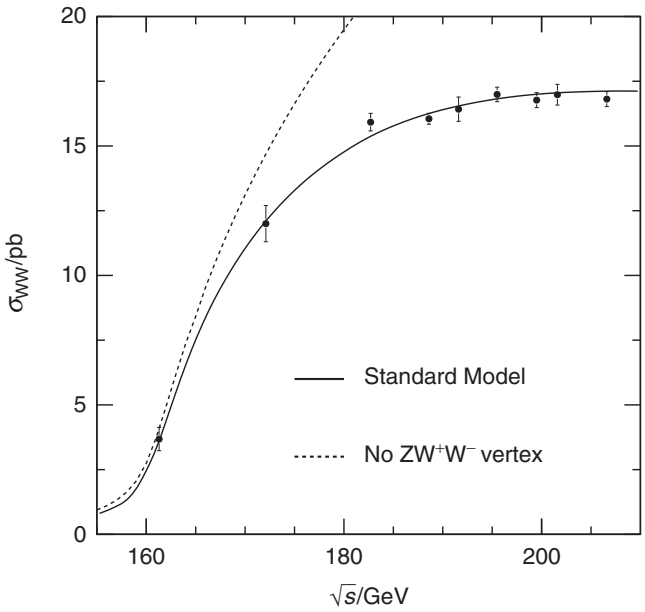

Fig. 16.10 The measurements of the $e^+e^- \rightarrow W^+W^-$ cross section at LEP. The curve shows the Standard Model prediction from the three Feynman diagrams of Figure 15.5. Also shown is the prediction without the Z-exchange diagram. The points show the combined results from the ALEPH, DELPHI, L3 and OPAL Collaborations.

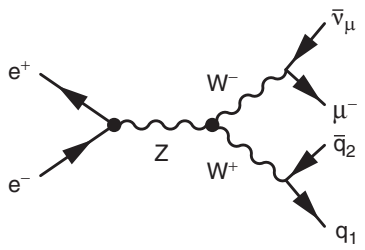

Fig. 16.11 One of the three Feynman diagrams for $e^+e^- \rightarrow W^+W^- \rightarrow \mu^-\bar{\nu}_\mu q_1\bar{q}_2$.

of the $e^+e^- \rightarrow W^+W^-$ cross section close to threshold at $\sqrt{s} \sim 2m_W$, where the position and sharpness of the turn-on of the cross section depend on m_W and Γ_W. Significantly above threshold, where the majority of the LEP data were recorded, m_W and Γ_W are determined from the *direct reconstruction* of the invariant masses of the W-decay products.

Up to this point, the production and decay of the W bosons in the process $e^+e^- \rightarrow W^+W^-$ have been discussed as independent processes. This distinction, which effectively treats the W bosons as real on-shell particles, is not strictly correct. The W bosons should be considered as virtual particles. For example, Figure 16.11 shows one of the three Feynman diagrams for $e^+e^- \rightarrow \mu^-\bar{\nu}_\mu q_1\bar{q}_2$, which proceeds via the production and decay of two virtual W bosons. In this

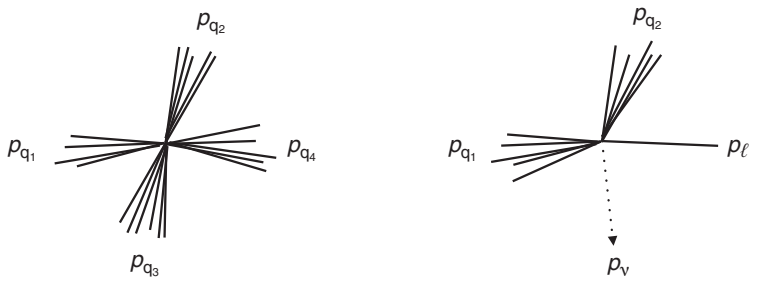

Fig. 16.12 The $WW \to qqqq$ and $WW \to q\bar{q}\ell\nu$ event topologies used at LEP to determine the W-boson mass from the direct reconstruction of the decay products.

diagram, there are three propagators, one for the Z boson and one for each of the two W bosons. The propagators for the virtual W bosons have the form

$$\frac{1}{q^2 - m_W^2 + im_W\Gamma_W},$$

where q is the four-momentum of the W boson and the imaginary term accounts for its finite lifetime. The contribution of the two W-boson propagators to the matrix element squared is therefore

$$|\mathcal{M}|^2 \propto \frac{1}{(q_1^2 - m_W^2)^2 + m_W^2\Gamma_W^2} \times \frac{1}{(q_2^2 - m_W^2)^2 + m_W^2\Gamma_W^2}, \tag{16.27}$$

where q_1 and q_2 are the four-momenta of the two W bosons. Hence, the invariant mass of the two fermions from each W-boson decay is not fixed to be exactly m_W, but will distributed as a Lorentzian centred on m_W with width Γ_W. A precise determination of the W-boson mass and width can be obtained from the direct reconstruction of the four-momenta of the four fermions in the $W^+W^- \to \ell\nu q_1\bar{q}_2$ and $W^+W^- \to q_1\bar{q}_2q_3\bar{q}_4$ decay topologies, shown in Figure 16.12.

For $W^+W^- \to q_1\bar{q}_2q_3\bar{q}_4$ decays, the measured four-momenta of the four jets can be used directly to reconstruct the invariant masses of the two W bosons,

$$m_1^2 = q_1^2 = (p_{q_1} + p_{q_2})^2 \quad \text{and} \quad m_2^2 = q_2^2 = (p_{q_3} + p_{q_4})^2.$$

The masses of the two W bosons produced in $W^+W^- \to \ell\nu q_1\bar{q}_2$ decays can be determined by reconstructing the momentum of the neutrino. Because the e^+e^- collisions occur in the centre-of-mass frame, the total four-momentum of the final-state particles is constrained to

$$P_{\text{tot}} = (\sqrt{s}, \mathbf{0}).$$

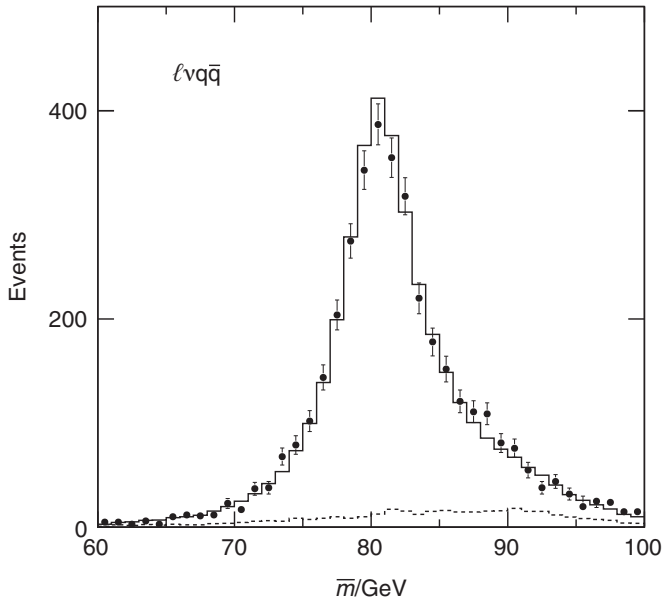

Fig. 16.13 The reconstructed invariant mass distribution of W bosons in $e^+e^- \to W^+W^- \to \ell\nu q\bar{q}$ events in the L3 experiment at LEP. The dashed line indicates the background from events other than $W^+W^- \to \ell\nu q\bar{q}$. Adapted from Achard *et al.* (2006).

Consequently, the neutrino four-momentum can be obtained from the measured four-momenta of the charged lepton and the two jets,

$$p_\nu = P_{\text{tot}} - p_\ell - p_{q_1} - p_{q_2}.$$

Thus, the masses of the two W bosons in the $W^+W^- \to \ell\nu q_1\bar{q}_2$ decays can be measured from

$$m_1^2 = q_1^2 = (p_{q_1} + p_{q_2})^2 \quad \text{and} \quad m_2^2 = q_2^2 = (p_\ell + p_\nu)^2.$$

Whilst jet angles are generally well reconstructed, the experimental jet energy resolution is relatively poor. The resolution on the reconstructed invariant masses in each observed event can be improved by using the constraint $P_{\text{tot}} = (\sqrt{s}, \mathbf{0})$, which implies that both W bosons will have half the centre-of-mass energy and will have equal and opposite three-momenta.

Figure 16.13 shows the reconstructed W-mass distribution for $\ell\nu q_1\bar{q}_2$ events observed in the L3 experiment. For each observed W^+W^- event, the average reconstructed W-boson mass $\overline{m} = \frac{1}{2}(m_1 + m_2)$ is plotted. The position of the peak determines m_W and the width of the distribution, after accounting for the experimental resolution, determines Γ_W. The results from the four LEP experiments give

$$m_W = 80.376 \pm 0.033\,\text{GeV} \quad \text{and} \quad \Gamma_W = 2.195 \pm 0.083\,\text{GeV}.$$

It is worth noting that, owing to the Lorentzian form of the propagator, the virtual W bosons in the Feynman diagram of Figure 16.11 tend to be produced in the

range $q^2 \sim (m_W \pm \Gamma_W)^2$ and are therefore usually close to being on-shell, as can be seen from (16.13). For this reason, the process $e^+e^- \to W^+W^- \to f_1\bar{f}_2f_3\bar{f}_4$ can be approximated as the production of two real W bosons, each of which subsequently decays to two fermions. For more accurate calculations, such as the Standard Model prediction shown in Figure 16.10, this approximation is not sufficient to match the experimental precision and the process has to be treated as the production of four fermions through two virtual W bosons.

16.3.2 Measurement of the W mass at the Tevatron

The study of W-boson pair production at LEP provides precise measurements of m_W, Γ_W and the W-boson branching ratios. Precision measurements can also be made at hadron colliders. For example, m_W has been measured precisely at the Tevatron in the process $p\bar{p} \to WX$, where X is the hadronic system from initial-state QCD radiation and the remnants of the colliding hadrons. In $p\bar{p}$ collisions, the W boson is produced in parton-level processes such as $u\bar{d} \to W^+ \to \mu^+\bar{\nu}_\mu$. In order to reconstruct the mass of the W boson, the momentum of the neutrino needs to be determined.

At a hadron collider, the centre-of-mass energy of the underlying $q\bar{q}'$ annihilation process is not known on an event-by-event basis. If x_1 and x_2 are the momentum fractions of the proton and antiproton carried by the annihilating q and $\bar{q}'$, the four-momentum of the final state is

$$P_{\text{tot}} = \left[(x_1 + x_2)\frac{\sqrt{s}}{2},\ 0,\ 0,\ (x_1 - x_2)\frac{\sqrt{s}}{2}\right].$$

Consequently, the final-state W boson will be boosted along the beam (z) axis. Because the momentum fractions x_1 and x_2 are unknown, the components of the momentum of the final-state system only balance in the transverse (xy) plane. The typical $W \to \mu\nu$ event topology, as seen in the plane transverse to the beam axis, is illustrated in the left plot of Figure 16.14. The transverse components of the momentum of the neutrino can be reconstructed from the transverse momentum of the muon, $\mathbf{p}_T^\mu = p_x\hat{\mathbf{x}} + p_y\hat{\mathbf{y}}$, and the (usually small) transverse momentum $\mathbf{u}_T$ of the hadronic system X,

$$\mathbf{p}_T^\nu = -\mathbf{p}_T^\mu - \mathbf{u}_T.$$

Owing to the unknown momentum fractions of the colliding partons, the z-component of the neutrino momentum cannot be determined.

Because the z-component of the momentum of the neutrino is unknown, the invariant mass of the products from the decaying W boson can not be determined on an event-by-event-basis. However, it is possible to define the transverse mass

$$m_T \equiv \left[2\left(p_T^\mu p_T^\nu - \mathbf{p}_T^\mu \cdot \mathbf{p}_T^\nu\right)\right]^{\frac{1}{2}}.$$

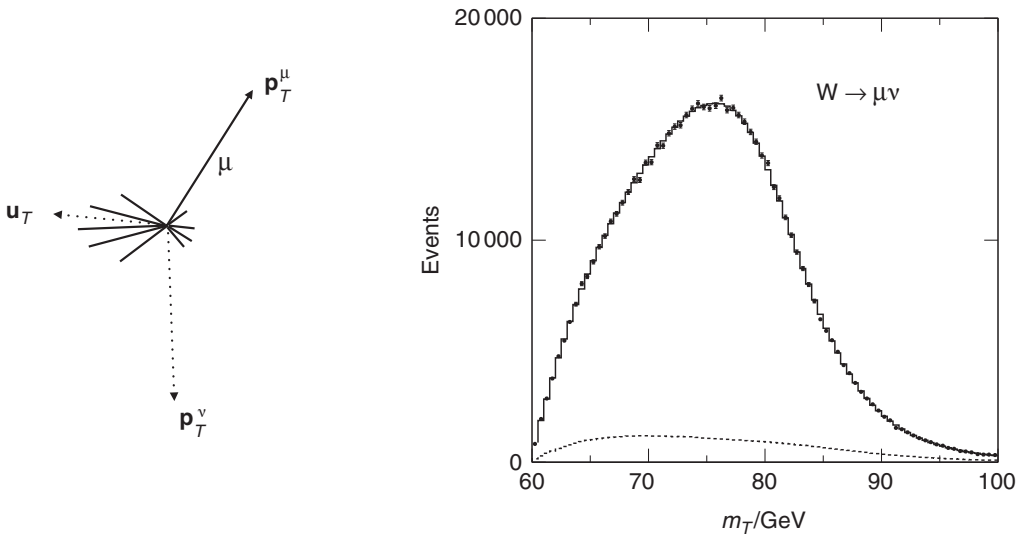

Fig. 16.14 The W → μν event topology for W bosons produced in $p\bar{p}$ collisions at the Tevatron and the reconstructed transverse mass distribution from the CDF experiment, adapted from Aaltonen *et al.* (2012).

Figure 16.14 shows the reconstructed m_T distribution from over 600 000 W → μν decays observed in the CDF detector. Because the longitudinal components of the momentum are not included, m_T does not peak at m_W and the distribution of m_T is relatively broad. Nevertheless, these disadvantages are outweighed by the very large W-production cross section at a hadron–hadron collider. Because of the large numbers of events, m_W can be measured even more precisely than at LEP. The sensitivity to m_W comes from the shape of the m_T distribution and the position of the broad peak. The combined results from the CDF and D0 experiments at the Tevatron and the four LEP experiments give

$$m_W = 80.385 \pm 0.015\,\text{GeV} \quad \text{and} \quad \Gamma_W = 2.085 \pm 0.042\,\text{GeV}.$$

16.4 Quantum loop corrections

The data from LEP, the Tevatron and elsewhere provide precise measurements of the fundamental parameters of the electroweak model. The masses of the weak gauge bosons are determined to be

$$m_Z = 91.1875 \pm 0.0021\,\text{GeV} \quad \text{and} \quad m_W = 80.385 \pm 0.015\,\text{GeV}.$$

The weak mixing angle is determined to be

$$\sin^2\theta_W = 0.23146 \pm 0.00012,$$

and the strengths of the weak and electromagnetic interaction are

$$G_{\mathrm{F}} = 1.166\,378\,7(6) \times 10^{-5}\,\mathrm{GeV}^{-2} \quad \text{and} \quad \alpha(m_{\mathrm{Z}}^2) = \frac{1}{128.91 \pm 0.02},$$

where α is given at the electroweak scale of $q^2 = m_{\mathrm{Z}}^2$. In the Standard Model, the masses of the W and Z bosons are not free parameters, they are determined by the Higgs mechanism, described in Chapter 17. Consequently, if any three of the parameters m_{Z}, m_{W}, G_{F}, α and $\sin^2\theta_{\mathrm{W}}$ are known, the other two are determined by exact relations from the electroweak unification mechanism of the Standard Model. For example, the mass of the W boson is related to α, G_{F} and θ_{W} by

$$m_{\mathrm{W}} = \left(\frac{\pi\alpha}{\sqrt{2}G_{\mathrm{F}}}\right)^{\frac{1}{2}} \frac{1}{\sin\theta_{\mathrm{W}}},$$

and the masses of the W and Z bosons are related by

$$m_{\mathrm{W}} = m_{\mathrm{Z}} \cos\theta_{\mathrm{W}}.$$

These constraints, coupled with the precise measurements described above, allow the electroweak sector of the Standard Model to be tested to high precision. For example, using the measurements of m_{Z} and $\sin^2\theta_{\mathrm{W}}$, the predicted mass of the W boson obtained from $m_{\mathrm{W}} = m_{\mathrm{Z}} \cos\theta_{\mathrm{W}}$ is

$$m_{\mathrm{W}}^{\mathrm{pred}} = 79.937 \pm 0.009\,\mathrm{GeV}.$$

Despite being of the right order, this prediction is thirty standard deviations smaller than the measured value of $m_{\mathrm{W}} = 80.385 \pm 0.015\,\mathrm{GeV}$. This apparent discrepancy does not represent a failure of the Standard Model; it can be explained by higher-order contributions from virtual quantum loop corrections. For example, the mass of the W boson includes contributions from virtual loops, of which the two largest are shown in Figure 16.15. As a result of these quantum loops, the physical W-boson mass differs from the lowest-order prediction m_{W}^0 by

$$m_{\mathrm{W}} = m_{\mathrm{W}}^0 + a\,m_{\mathrm{t}}^2 + b \ln\left(\frac{m_{\mathrm{H}}}{m_{\mathrm{W}}}\right) + \cdots, \tag{16.28}$$

where a and b are calculable constants, and m_{t} and m_{H} are the masses of the top quark and Higgs boson.

The difference between the predicted lowest-order W-boson mass and the measured value effectively measures the size of these quantum loop corrections. Since the dependence on the Higgs mass is only logarithmic, the dominant correction in (16.28) comes from the top quark mass. In 1994 the measurements of the electroweak parameters at LEP implied a top quark mass of $175 \pm 11\,\mathrm{GeV}$. Shortly afterwards, the top quark was discovered at the Tevatron with a mass consistent

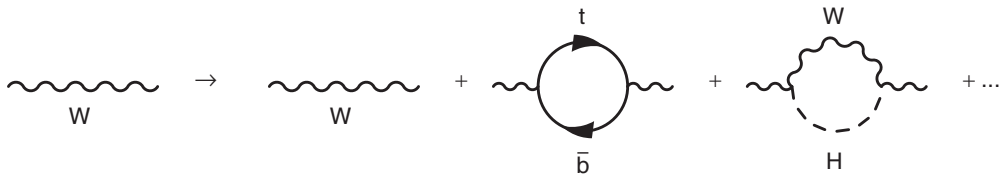

Fig. 16.15 The two largest loop corrections to the W mass.

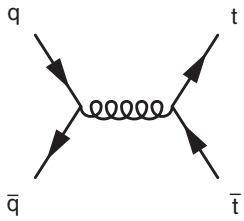

Fig. 16.16 The lowest-order Feynman diagram for $t\bar{t}$ production in $p\bar{p}$ collisions at the Tevatron.

with this prediction. This direct observation of the effects of quantum loop corrections provides an impressive validation of the electroweak sector of the Standard Model.

Because the electroweak measurements are sufficiently precise to be sensitive to quantum loop corrections, they strongly constrain possible models for physics beyond the Standard Model; any new particle or interaction that gives rise to a significant contribution to the quantum loop corrections to the W-boson mass will not be consistent with the experimental data.

16.5 The top quark

The top quark is by some way the most massive of the quarks. In fact, with a mass of approximately 175 GeV, it is the most massive fundamental particle in the Standard Model, $m(\mathrm{t}) > m(\mathrm{H}) > m(\mathrm{Z}) > m(\mathrm{W})$. Because of its mass, the top quark could not be observed directly at LEP and was only discovered in 1994 in $p\bar{p}$ collisions at the Tevatron. In $p\bar{p}$ collisions, top quarks are predominantly produced in pairs in the QCD process $q\bar{q} \to t\bar{t}$, shown in Figure 16.16.

Owing to its large mass, the lifetime of the top quark is very short. Consequently, the top pairs produced in the process $q\bar{q} \to t\bar{t}$ do not have time to form bound states, such as those observed in the resonant production of charmonium ($c\bar{c}$) and bottomonium ($b\bar{b}$) states (discussed in Section 10.8). Because $|V_{tb}| \gg |V_{ts}| > |V_{td}|$, the top quark decays almost entirely by $t \to bW^+$. Hence top quark pair production and decay at the Tevatron (and at the LHC) proceeds mostly by

$$q\bar{q} \to t\bar{t} \to bW^+ \bar{b}W^-.$$

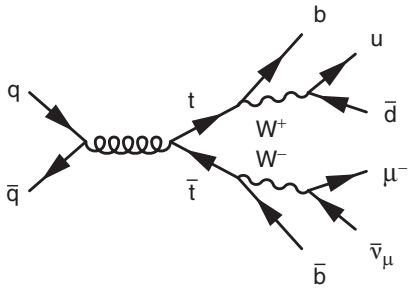

Fig. 16.17 The lowest-order Feynman diagram for $t\bar{t}$ production in $p\bar{p}$ collisions, where the W bosons decay to give a semi-leptonic final state.

The Feynman diagram for the production of the $t\bar{t}$ semi-leptonic final state, where one W boson decays leptonically and the other decays hadronically, is shown in Figure 16.17. The corresponding matrix element contains four propagators for massive particles, two for the top quarks and two for the W bosons. Because $\Gamma_W \ll m_W$, the largest contributions to the matrix element will be when the W bosons are produced almost on-shell with $q^2 \sim m_W^2$. Similarly, the presence of the propagators for the two virtual top quarks implies that

$$|\mathcal{M}|^2 \propto \frac{1}{(q_1^2 - m_t^2)^2 + m_t^2\Gamma_t^2} \times \frac{1}{(q_2^2 - m_t^2)^2 + m_t^2\Gamma_t^2}.$$

As a result, the invariant masses of each of the W^+b and $W^-\bar{b}$ systems, produced in the top decays, will be distributed according Lorentzian centred on m_t with width Γ_t.

16.5.1 Decay of the top quark

Because the W boson from the decay of a top quark is close to being on-shell, $q^2 \sim m_W^2$, the top decay width can be calculated from the Feynman diagram for $t \to bW^+$ shown in Figure 16.18, where the W boson is treated as a real on-shell final-state particle. The corresponding matrix element is obtained from the quark spinors, the weak charged-current vertex factor and the term $\epsilon^*(p_W)$ for the polarisation state of the W boson,

$$-i\mathcal{M} = \left[\overline{u}(p_b)\,\frac{-ig_W}{\sqrt{2}}\gamma^\mu\tfrac{1}{2}(1-\gamma^5)\,u(p_t)\right] \times \epsilon_\mu^*(p_W),$$

and thus

$$\mathcal{M} = \tfrac{g_W}{\sqrt{2}}\,\epsilon_\mu^*(p_W)\,\overline{u}(p_b)\gamma^\mu\tfrac{1}{2}(1-\gamma^5)u(p_t). \tag{16.29}$$

It is convenient to consider the decay in the rest frame of the top quark and to take the final-state b-quark direction to define the z-axis. Neglecting the mass of the b-quark, the four-momenta of the t, b and W^+ can be written

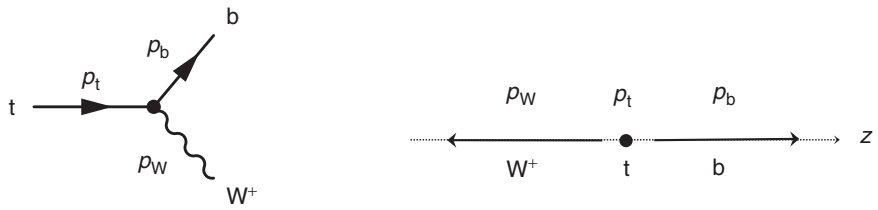

Fig. 16.18 The lowest-order Feynman diagram for the decay $t \rightarrow bW^+$ and coordinates used for the calculation of the decay rate.

$$p_t = (m_t, 0, 0, 0), \quad p_b = (p^*, 0, 0, p^*) \quad \text{and} \quad p_W = (E^*, 0, 0, -p^*),$$

where p^* is the magnitude of the momentum of the final-state particles in the centre-of-mass frame and E^* is the energy of the W boson, $E^{*2} = (p^*)^2 + m_W^2$. The weak interaction couples only to left-handed chiral particle states. Here, in the limit $p^* \gg m_b$, the chiral states are equivalent to the helicity states and, consequently, the b-quark can only be produced in a left-handed helicity state such that for the configuration of Figure 16.18 its spin points in the negative z-direction. Hence, the matrix element of (16.29) can be written as

$$\mathcal{M} = \frac{g_W}{\sqrt{2}} \epsilon_\mu^*(p_W)\, \bar{u}_\downarrow(p_b)\gamma^\mu u(p_t). \tag{16.30}$$

From (4.67), the LH helicity spinor for the b-quark is

$$u_\downarrow(p_b) \approx \sqrt{p^*} \begin{pmatrix} 0 \\ 1 \\ 0 \\ -1 \end{pmatrix}.$$

The two possible spin states of the top quark can be written using the u_1 and u_2 spinors, which for a top quark at rest are (4.48),

$$u_1(p_t) = \sqrt{2m_t} \begin{pmatrix} 1 \\ 0 \\ 0 \\ 0 \end{pmatrix} \quad \text{and} \quad u_2(p_t) = \sqrt{2m_t} \begin{pmatrix} 0 \\ 1 \\ 0 \\ 0 \end{pmatrix},$$

respectively representing $S_z = +\frac{1}{2}$ and $S_z = -\frac{1}{2}$ states. The four-vector quark currents for the two possible spin states, calculated using the relations of (6.12)–(6.15), are

$$j_1^\mu = \bar{u}_\downarrow(p_b)\gamma^\mu u_1(p_t) = \sqrt{2m_t p^*}(0, -1, -i, 0),$$
$$j_2^\mu = \bar{u}_\downarrow(p_b)\gamma^\mu u_2(p_t) = \sqrt{2m_t p^*}(1, 0, 0, 1).$$

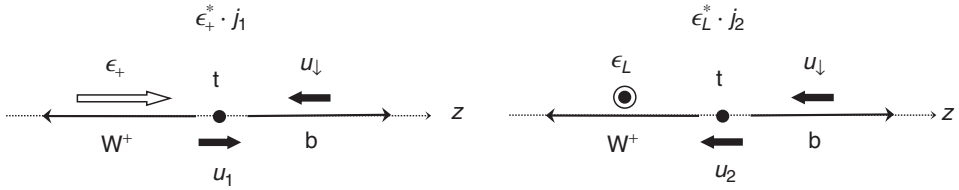

Fig. 16.19 The two allowed spin combinations in the process $t \to bW^+$.

The three possible polarisation states of the W boson, given by (15.1), are

$$\epsilon_+^*(p_W) = -\tfrac{1}{\sqrt{2}}(0, 1, -i, 0),$$
$$\epsilon_-^*(p_W) = \tfrac{1}{\sqrt{2}}(0, +1, +i, 0),$$
$$\epsilon_L^*(p_W) = \tfrac{1}{m_W}(-p^*, 0, 0, E^*),$$

which correspond to the $S_z = \pm 1$ and the longitudinal polarisation states. For a particular top quark spin and W polarisation state, the matrix element of (16.30) is given by the four-vector scalar product

$$\mathcal{M} = \tfrac{g_W}{\sqrt{2}} j_i \cdot \epsilon_\lambda^*.$$

The only combinations of the two possible quark currents and the three possible W-boson polarisations for which the matrix element is non-zero are $\epsilon_+^* \cdot j_1$ and $\epsilon_L^* \cdot j_2$. These two combinations correspond to the spin states shown in Figure 16.19, which (unsurprisingly) are the only configurations that conserve angular momentum.

The matrix elements for these two allowed spin configurations are

$$\mathcal{M}_1 = \frac{g_W}{\sqrt{2}} \epsilon_+^* \cdot j_1 = -\tfrac{g_W}{\sqrt{2}} \sqrt{m_t p^*}\,(0, 1, i, 0) \cdot (0, -1, -i, 0) = -g_W \sqrt{2 m_t p^*},$$
$$\mathcal{M}_2 = \frac{g_W}{\sqrt{2}} \epsilon_L^* \cdot j_2 = \tfrac{g_W}{m_W} \sqrt{m_t p^*}\,(-p^*, 0, 0, E^*) \cdot (1, 0, 0, 1) = -\frac{g_W}{m_W} \sqrt{m_t p^*}(E^* + p^*).$$

From conservation of energy, $E^* + p^* = m_t$, and therefore the spin-averaged matrix element squared for the decay $t \to bW^+$ is

$$\langle |\mathcal{M}^2| \rangle = \tfrac{1}{2}\left(|\mathcal{M}_1^2| + |\mathcal{M}_2^2|\right) = \tfrac{1}{2} g_W^2 m_t p^* \left(2 + \frac{m_t^2}{m_W^2}\right),$$

where the factor of one half averages over the two spin states of the t-quark. The total decay rate is obtained by substituting the spin-averaged matrix element into the formula of (3.49) which, after integrating over the 4π of solid angle, gives

$$\Gamma(t \to bW^+) = \frac{p^*}{8\pi m_t^2} \langle |\mathcal{M}^2| \rangle = \frac{g_W^2 p^{*2}}{16\pi m_t} \left(2 + \frac{m_t^2}{m_W^2}\right). \tag{16.31}$$

With some algebraic manipulation (see Problem 16.10), this can be written as

$$\Gamma(t \to bW^+) = \frac{G_F m_t^3}{8\sqrt{2}\pi}\left(1 - \frac{m_W^2}{m_t^2}\right)^2\left(1 + \frac{2m_W^2}{m_t^2}\right), \tag{16.32}$$

where g_W^2 is given in terms of the Fermi constant, $G_F = \sqrt{2}g_W^2/(8m_W^2)$. For the measured values of $m_t = 173\,\text{GeV}$, $m_W = 80.4\,\text{GeV}$ and $G_F = 1.166 \times 10^{-5}\,\text{GeV}^{-2}$, the lowest-order calculation of the total decay width of the top quark gives

$$\Gamma_t = 1.5\,\text{GeV}. \tag{16.33}$$

Hence the top quark lifetime is of order $\tau_t = 1/\Gamma_t \approx 5 \times 10^{-25}$ s. This is sufficiently short that the top quarks produced at the Tevatron decay in a distance of order 10^{-16} m. This is small compared to the typical length scale for the hadronisation process, and therefore the $t\bar{t}$ pairs produced at the Tevatron not only decay before forming a bound state, but also decay before hadronising.

16.5.2 Measurement of the top quark mass

The mass of the top quark has been measured in the process $p\bar{p} \to t\bar{t}$ by direct reconstruction of the top quark decay products, similar to the procedure used to measure the W-boson mass at LEP. Since both top quarks decay to a b-quark and a W boson there are three distinct final-state topologies:

$t\bar{t} \to (bW^+)(\bar{b}W^-) \to (b\,q_1\bar{q}_2)\,(\bar{b}\,q_3\bar{q}_4) \to 6$ jets,

$t\bar{t} \to (bW^+)(\bar{b}W^-) \to (b\,q_1\bar{q}_2)\,(\bar{b}\,\ell^-\bar{\nu}_\ell) \to 4$ jets + 1, charged lepton + 1ν

$t\bar{t} \to (bW^+)(\bar{b}W^-) \to (b\,\ell^+\nu_\ell)\,(\bar{b}\,\ell'^-\bar{\nu}_{\ell'}) \to 2$ jets + 2 charged leptons + 2νs.

The measurement of the top quark mass is more complicated than the corresponding measurement of the W-mass at LEP, but the principle is the same. The b-quark jets are identified from the tagging of secondary vertices (see Section 1.3.1) and the remaining jets have to be associated to the W-boson decay(s), as indicated in Figure 16.20. Because the momentum of the $t\bar{t}$ system in the beam (z) direction is not known (see Section 16.3.2), it might appear that there is insufficient information to fully reconstruct the neutrino momentum in observed $t\bar{t} \to$ four jets + ℓ + ν events. However, the invariant mass of the two jets associated with a W boson and the invariant mass of the lepton and neutrino both can be constrained to m_W within $\pm\Gamma_W$. Furthermore, the invariant masses of the particles forming the two reconstructed top quarks can be required to be equal. These additional constraints provide a system of equations that allow the momentum of the neutrino to be determined from the technique of kinematic fitting. In both the fully hadronic and $t\bar{t} \to$ four jets + ℓ + ν decay topologies, these constraints improve the event-by-event mass resolution.

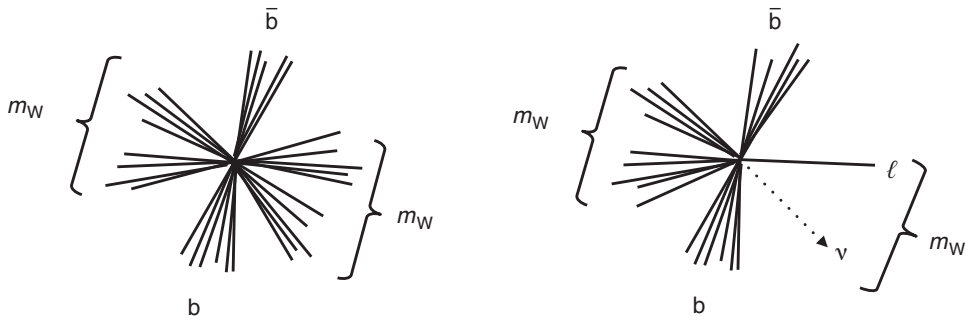

Fig. 16.20 The two main $t\bar{t}$ event topologies used at the Tevatron to determine the top quark mass from the direct reconstruction of the decay products.

The top quark mass has been determined by both the CDF and D0 collaborations using the measured four-momenta of the jets and leptons in observed $t\bar{t} \to$ six jets and $t\bar{t} \to$ four jets + ℓ + ν events. As an example, Figure 16.21 shows the reconstructed top mass distribution from an analysis of data recorded by the CDF experiment. Whilst the reconstructed mass peak is relatively broad due to experimental resolution, a clear peak is observed allowing the top mass to be determined with a precision of $O(1\%)$. The current average of the top quark mass measurements from the CDF and D0 experiments is

$$m_t = 173.5 \pm 1.0\,\text{GeV}.$$

The total width of the top quark is measured to be $\Gamma_t = 2.0 \pm 0.6\,\text{GeV}$. The top width is determined much less precisely than the top quark mass because the width of the distribution in Figure 16.21 is dominated by the experimental resolution. Nevertheless, the current measurement is consistent with the result of the lowest-order calculation presented in Section 16.5.1.

A window on the Higgs boson

Just as the electroweak measurements at LEP provided a prediction of the top quark mass through its quantum loop corrections to the W-boson mass, the precise determination of the top quark mass at the Tevatron provides a window on the Higgs boson. Its measurement determines the size of the largest loop correction to the W-boson mass, which arises from the virtual $t\bar{b}$ loop in Figure 16.15. The next largest correction arises from the WH loop that leads to the logarithmic term in (16.28). The electroweak measurements at LEP and the Tevatron, when combined with the direct measurement of the top quark mass, constrain the mass of the Standard Model Higgs boson to be in the range

$$50\,\text{GeV} \lesssim m_H \lesssim 150\,\text{GeV}.$$

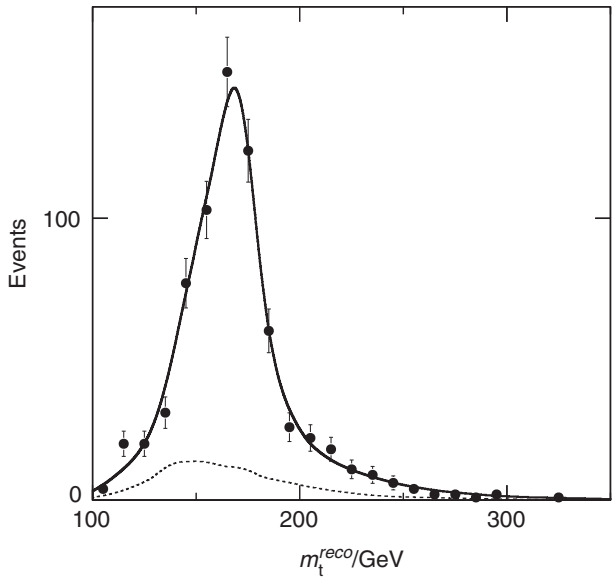

Fig. 16.21 The distribution of the reconstructed top mass in selected $t\bar{t} \rightarrow$ four jets $+ \ell + \nu$ events in the CDF detector at the Tevatron. The dashed curve indicates the expected contribution from processes other than $t\bar{t}$. Adapted from Aaltonen *et al.* (2011).

Direct searches for the Higgs boson at LEP placed a lower bound on its mass of

$$m_{\mathrm{H}} > 115\,\mathrm{GeV}.$$

Hence, prior to the turn-on of the LHC, the window for the Standard Model Higgs boson was already quite narrow.

Summary

The Z boson was studied with very high precision at the LEP e^+e^- collider. The resulting measurements provided a stringent test of the predictions of the GSW model for electroweak unification. The mass of the Z boson, which is a fundamental parameter of the Standard Model, was determined to be

$$m_{\mathrm{Z}} = 91.1875 \pm 0.0021\,\mathrm{GeV}.$$

The observed couplings of the Z boson are consistent with the Standard Model expectations with

$$\sin^2\theta_{\mathrm{W}} = 0.23146 \pm 0.00012.$$

The measurements of Γ_Z and the $e^+e^- \to Z \to f\bar{f}$ cross sections, demonstrate that there are only three generations of light neutrinos (assuming standard couplings), which is strongly suggestive that there are only three generations of fundamental fermions. Furthermore, studies of the W boson at LEP and the Tevatron and the studies of the top quark at the Tevatron, show that

$$m_W = 80.385 \pm 0.015\,\text{GeV} \quad \text{and} \quad m_t = 173.5 \pm 1.0\,\text{GeV}.$$

Remarkably, when combined, the above measurements of the electroweak sector of the Standard Model are sufficiently precise to reveal effects at the quantum loop level. These precision measurements and the ability of the Standard Model to describe the electroweak data, represent one of the highlights of modern physics. However, there is a serious problem with the Standard Model as it has been presented so far; the fact the W and Z bosons have mass breaks the required gauge symmetry of the Standard Model. The solution to this apparent contradiction is the Higgs mechanism.

Problems

16.1 After correcting for QED effects, including initial-state radiation, the measured $e^+e^- \to \mu^+\mu^-$ and $e^+e^- \to$ hadrons cross sections at the peak of the Z resonance give

$$\sigma^0(e^+e^- \to Z \to \mu^+\mu^-) = 1.9993\,\text{nb} \quad \text{and} \quad \sigma^0(e^+e^- \to Z \to \text{hadrons}) = 41.476\,\text{nb}.$$

(a) Assuming lepton universality, determine $\Gamma_{\ell\ell}$ and Γ_{hadrons}.
(b) Hence, using the measured value of $\Gamma_Z = 2.4952 \pm 0.0023$ GeV and the theoretical value of $\Gamma_{\nu\nu}$ given by Equation (15.41), obtain an estimate of the number of light neutrino flavours.

16.2 Show that the $e^+e^- \to Z \to \mu^+\mu^-$ differential cross section can be written as

$$\frac{d\sigma}{d\Omega} \propto (1 + \cos^2\theta) + \tfrac{8}{3}A_{FB}\cos\theta.$$

16.3 From the measurement of the muon asymmetry parameter,

$$\mathcal{A}_\mu = 0.1456 \pm 0.0091,$$

determine the corresponding value of $\sin^2\theta_W$.

16.4 The e^+e^- Stanford Linear Collider (SLC), operated at $\sqrt{s} = m_Z$ with left- and right-handed longitudinally polarised beams. This enabled the $e^+e^- \to Z \to f\bar{f}$ cross section to be measured separately for left-handed and right-handed electrons.

Assuming that the electron beam is 100% polarised and that the positron beam is unpolarised, show that the left–right asymmetry A_{LR} is given by

$$A_{LR} = \frac{\sigma_L - \sigma_R}{\sigma_L + \sigma_R} = \frac{(c_L^e)^2 - (c_R^e)^2}{(c_L^e)^2 + (c_R^e)^2} = \mathcal{A}_e,$$

where σ_L and σ_R are respectively the measured cross sections at the Z resonance for LH and RH electron beams.

16.5 From the expressions for the matrix elements given in (16.8), show that:

(a) the average polarisation of the tau leptons produced in the process $e^+e^- \to Z \to \tau^+\tau^-$ is

$$\langle P_{\tau^-} \rangle = \frac{N_\uparrow - N_\downarrow}{N_\uparrow + N_\downarrow} = -\mathcal{A}_\tau,$$

where $N_\uparrow$ and $N_\downarrow$ are the respective numbers of τ^- produced in RH and LH helicity states;

(b) the tau polarisation where the τ^- is produced at an angle θ with respect to the initial-state e^- is

$$P_{\tau^-}(\cos\theta) = \frac{N_\uparrow(\cos\theta) - N_\downarrow(\cos\theta)}{N_\uparrow(\cos\theta) + N_\downarrow(\cos\theta)} = -\frac{\mathcal{A}_\tau(1+\cos^2\theta) + 2\mathcal{A}_e\cos\theta}{(1+\cos^2\theta) + \frac{8}{3}A_{FB}\cos\theta}.$$

16.6 The average tau polarisation in the process $e^+e^- \to Z \to \tau^+\tau^-$ can be determined from the energy distribution of π^- in the decay $\tau^- \to \pi^-\nu_\tau$. In the τ^- rest frame, the π^- four-momentum can be written $p = (E^*, p^* \sin\theta^*, 0, p^* \cos\theta^*)$, where θ^* is the angle with respect to the τ^- spin, and the differential partial decay width is

$$\frac{d\Gamma}{d\cos\theta^*} \propto \frac{(p^*)^2}{m_\tau}(1+\cos\theta^*).$$

(a) Without explicit calculation, explain this angular dependence.

(b) For the case where the τ^- is right-handed, show that the observed energy distribution of the π^- *in the laboratory frame* is

$$\frac{d\Gamma_{\tau^-_\uparrow}}{dE_{\pi^-}} \propto x,$$

where $x = E_\pi/E_\tau$.

(c) What is the corresponding π^- energy distribution for the decay of a LH helicity τ^-.

(d) If the observed pion energy distribution is consistent with

$$\frac{d\Gamma}{dx} = 1.14 - 0.28x \equiv 0.86x + 1.14(1-x),$$

determine $\mathcal{A}_\tau$ and the corresponding value of $\sin^2\theta_W$.

16.7 There are ten possible lowest-order Feynman diagrams for the process $e^+e^- \to \mu^-\nu_\mu u\bar{d}$, of which only three involve a W^+W^- intermediate state. Draw the other seven diagrams (they are all *s*-channel processes involving a single virtual W).

16.8 Draw the two lowest-order Feynman diagrams for $e^+e^- \to ZZ$.

16.9 In the OPAL experiment at LEP, the efficiencies for selecting $W^+W^- \to \ell\nu q_1\bar{q}_2$ and $W^+W^- \to q_1\bar{q}_2q_3\bar{q}_4$ events were 83.8% and 85.9% respectively. After correcting for background, the observed numbers of $\ell\nu q_1\bar{q}_2$ and $q_1\bar{q}_2q_3\bar{q}_4$ events were respectively 4192 and 4592. Determine the measured value of the W-boson hadronic branching ratio $BR(W \to q\bar{q}')$ and its statistical uncertainty.

16.10 Suppose the four jets in an identified $e^+e^- \to W^+W^-$ event at LEP are measured to have momenta,

$$p_1 = 82.4 \pm 5\,\text{GeV},\ p_2 = 59.8 \pm 5\,\text{GeV},\ p_3 = 23.7 \pm 5\,\text{GeV} \text{ and } p_4 = 42.6 \pm 5\,\text{GeV},$$

and directions given by the Cartesian unit vectors,

$$\hat{\mathbf{n}}_1 = (0.72, 0.33, 0.61), \quad \hat{\mathbf{n}}_2 = (-0.61, 0.58, -0.53),$$
$$\hat{\mathbf{n}}_3 = (-0.63, -0.72, -0.25), \quad \hat{\mathbf{n}}_4 = (-0.14, -0.96, -0.25).$$

Assuming that the jets can be treated as massless particles, find the most likely association of the four jets to the two W bosons and obtain values for the invariant masses of the (off-shell) W bosons in this event. Optionally, calculate the uncertainties on the reconstructed masses assuming that the jet directions are perfectly measured.

16.11 Show that the momenta of the final-state particles in the decay $t \to W^+ b$ are

$$p^* = \frac{m_t^2 - m_W^2}{2m_t},$$

and show that the decay rate of (16.31) leads to the expression for Γ_t given in (16.32).